Power Scaling for Collimated γ-Ray Beams Generated by Structured Laser-Irradiated Targets and Its Application to Two-Photon Pair Production

T. Wang,[1,2] X. Ribeyre,[3] Z. Gong,[4] O. Jansen,[1] E. d'Humières,[3] D. Stutman,[5,6] T. Toncian,[7] and A. Arefiev[1,2,*]

[1] *Department of Mechanical and Aerospace Engineering, University of California at San Diego, La Jolla, California 92093, USA*

[2] *Center for Energy Research, University of California at San Diego, La Jolla, California 92093, USA*

[3] *Univ. Bordeaux-CNRS-CEA, Centre Lasers Intenses et Applications, UMR 5107, 33405 Talence, France*

[4] *Center for High Energy Density Science, The University of Texas, Austin, Texas 78712, USA*

[5] *Extreme Light Infrastructure-Nuclear Physics (ELI-NP)/Horia Hulubei National Institute of Physics and Nuclear Engineering, 077125 Bucharest-Magurele, Romania*

[6] *Department of Physics and Astronomy, Johns Hopkins University, Baltimore, Maryland 21218, USA*

[7] *Institute for Radiation Physics, Helmholtz-Zentrum Dresden-Rossendorf e.V., 01328 Dresden, Germany*

(Received 18 August 2019; revised manuscript received 25 February 2020; accepted 14 April 2020; published 11 May 2020)

Using three-dimensional kinetic simulations, we examine the emission of collimated γ-ray beams from structured laser-irradiated targets with a prefilled cylindrical channel and its scaling with laser power (in the multi-PW range). The laser power is increased by increasing the laser energy and the size of the focal spot while keeping the peak intensity fixed at 5×10^{22} W/cm^2. The channel radius is increased proportionally to accommodate the change in laser spot size. The efficiency of conversion of the laser energy into a beam of MeV-level γ rays (with a 10° opening angle) increases rapidly with the incident laser power P before it roughly saturates above $P \approx 4$ PW. Detailed particle tracking reveals that the power scaling is a result of enhanced electron acceleration at higher laser powers. One application that directly benefits from such a strong scaling is pair production via two-photon collisions. We investigate two schemes for generating pairs through the linear Breit-Wheeler process: colliding two γ-ray beams and colliding one γ-ray beam with black-body radiation. The two scenarios project up to 10^4 and 10^5 pairs, respectively, for the γ-ray beams generated at $P = 4$ PW. A comparison with a regime of laser-irradiated hollow channels corroborates the robustness of the setup with prefilled channels.

DOI: 10.1103/PhysRevApplied.13.054024

I. INTRODUCTION

Over the past decade, x-ray free-electron lasers (XFELs) [1,2] have revolutionized multiple areas of science and technology by providing unprecedented sources of photons for detailed diagnostics of fast processes. For example, the European XFEL delivers over 10^{11} photons with energies in the region of 10 keV as a directed beam [3]. The underlying mechanism of operation of an XFEL is the emission of photons by a multi-GeV energetic electron beam that is periodically deflected by the magnetic field of an undulator. The next challenge is to develop a source of dense γ-ray beams with photon energies in the multi-MeV range, but upscaling the existing technology used at XFEL facilities may not be feasible. Increasing the energy of the emitted photons while maintaining a comparable photon yield would require a significant magnetic field increase. The desired field strength is well beyond what can be achieved, even with the use of superconducting undulators [4]. It is then appropriate to ask whether other technological developments can be leveraged to overcome this limitation.

One option is to use high-power high-intensity laser beams to drive extreme magnetic fields [5,6]. High-intensity laser pulses are capable of making a dense and otherwise opaque material transparent by heating electrons to relativistic energies. The heating increases the cutoff electron density for a given laser frequency; this is often referred to as relativistically induced transparency [7–9]. This effect allows the laser pulse to interact volumetrically with a dense plasma and drive strong currents capable of sustaining magnetic fields that are hundreds of kilotesla in strength [10–13]. Strong quasistatic magnetic fields enable efficient generation of γ rays inside the laser-irradiated plasma by not only inducing photon emission [11,12] but also enhancing the laser-driven electron

*aarefiev@eng.ucsd.edu

acceleration [14,15]. Multiple promising configurations involving high-intensity lasers have already been explored in the context of laser-driven electron acceleration [16,17] and photon emission [18–27]. Here our focus is on the interplay between the laser pulse and the laser-driven magnetic field in the structured targets that have started being used in experiments [28–30]. It has been shown that a static azimuthal magnetic field in a plasma can boost the electron energy gain to the GeV level [14].

We have previously examined electron acceleration and photon emission for a PW-class laser pulse with the parameters projected for the Texas PW laser system [31]. Using three-dimensional (3D) particle-in-cell (PIC) simulations, we found that large numbers of multi-MeV photons can be emitted even at a laser intensity of 5×10^{22} W/cm^2 [11] as a well-directed beam due to the presence of a strong azimuthal plasma magnetic field. Such a collimated γ-ray beam with a high photon flux provides a source uniquely suitable for studies of two-photon physics [32].

In the present work, we investigate how the γ-ray emission and the associated two-photon pair production scale with the incident laser power using 3D kinetic simulations. The laser power is increased by increasing the laser energy and the size of the focal spot while keeping the peak intensity fixed at 5×10^{22} W/cm^2. This scaling is a matter of significance, since it provides quantitative predictions across multi-PW to 10-PW-class laser platforms [33]. Note that technological challenges [34] exist when multi-PW beams are focused to higher intensities, and so it is meaningful to explore the power scaling at a fixed laser intensity. A peak intensity of approximately 5×10^{22} W/cm^2 is expected, for instance, with the 10-PW ELI-NP laser, after focusing with a $F/3$ parabolic mirror and reflecting the beam off a single plasma mirror [35]. Previously published studies have examined the electron energy gain and γ-ray emission by scanning over the laser peak intensity or the laser amplitude only [11,14,20,36,37]. The impact of the incident power for a fixed intensity has not been addressed. The present study is needed because it is not immediately clear how to extrapolate the results obtained for a 1-PW laser pulse to multi-PW pulses with the same peak intensity. In addition, we investigate the application of the resulting γ-ray beams to pair production via two-photon collisions and the scaling of the pair yield with power for two approaches: one is to collide two identical γ-ray beams [32], while the other is to collide one γ-ray beam with high-temperature black-body radiation [38].

We find that the efficiency of conversion of energy into multi-MeV photons emitted into a narrow cone (10° opening angle) increases rapidly with the incident laser power P for $P \leq 4$ PW. The conversion efficiency saturates above $P \approx 4$ PW as the system reaches optimal conditions for direct laser acceleration of electrons that emit energetic γ rays. The pair yields obtained through the two approaches scale differently with power, but both methods produce a considerable amount of pairs; e.g., colliding two γ-ray beams generated at $P = 4$ PW produces 10^4 pairs, whereas colliding such a beam with 400-eV black-body radiation produces 10^5 pairs.

The rest of the manuscript consists of five sections. In Sec. II, we discuss a baseline simulation for a 1-PW laser pulse. In Sec. III, we present results of a scan over the incident laser power P for an optimal plasma density of $20n_{cr}$ in the channel. In Sec. IV, we apply the γ-ray sources discussed here to calculate the electron-positron pair yield from two-photon collisions. Finally, in Sec. V, we summarize our results and discuss the implications of our findings.

II. BASELINE CASE—PHOTON EMISSION DRIVEN BY A 1-PW LASER PULSE

Photon emission from a structured target irradiated by a PW-level laser pulse has been previously investigated, and the results indicate that γ rays are efficiently emitted in the form of a well-directed beam [11]. In this section, we review the key features of this regime.

The setup utilizing a structured target is shown in Fig. 1(a), where the target contains a cylindrical channel filled with a material that becomes more transparent than the bulk when irradiated by an intense laser pulse. The channel effectively serves as an optical waveguide for the laser pulse, which is focused at the channel entrance. In our simulations, we choose the channel diameter to be comparable to that of the focal spot of the laser in order to reduce the reflection off the bulk material, allowing most of the laser energy to enter the target through the channel. As the laser beam propagates through the channel, it drives a longitudinal electron current that generates and sustains a quasistatic azimuthal magnetic field (see, e.g., Refs. [11–13]).

The plasma-generated magnetic field plays two important roles: it enhances the energy gain of the laser-accelerated electrons and it induces emission of γ rays by deflecting energetic electrons [11,14]. The synergy of these two processes in the channel leads to a significant enhancement of the γ-ray yield compared with the regime where the interaction is restricted to the target surface and the regime of near-vacuum interaction, where collective magnetic fields play no role. Figure 1(b) shows a representative electron trajectory in the azimuthal quasistatic magnetic field: the electron energy increases along the trajectory, which leads to emission of MeV-level photons, shown by arrows.

The choice of the bulk and channel materials is dictated by the peak amplitude E_0 of the electric field in the incoming laser pulse. The laser pulse quickly ionizes the irradiated material and turns it into a plasma, so that the optical properties are determined by the electron density n_e in the resulting plasma. The property that is important for

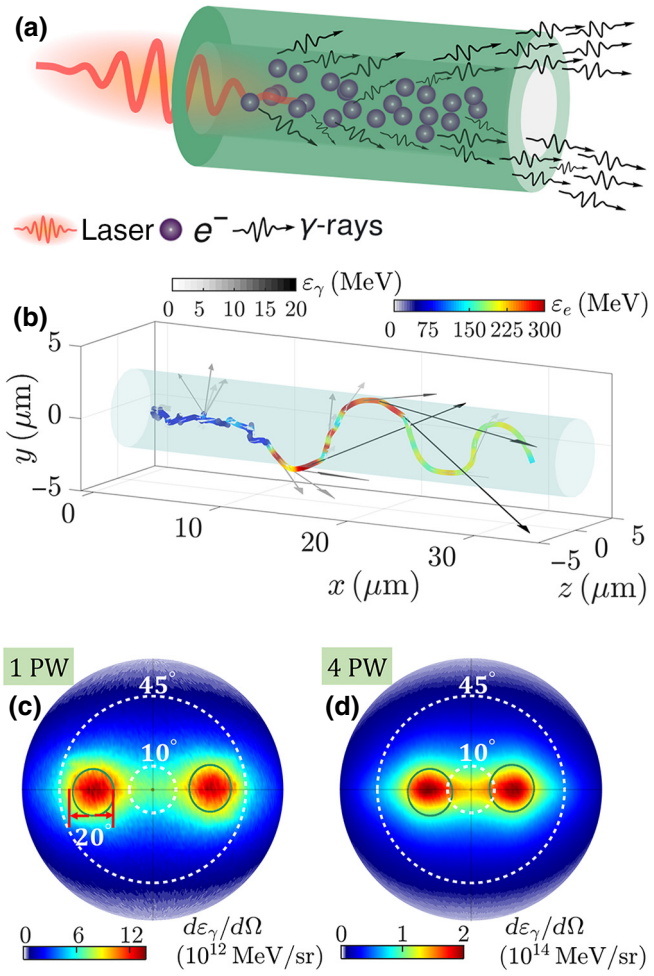

FIG. 1. (a) Schematic setup for generation of a directed γ-ray beam from a laser-irradiated structured target. (b) Representative electron trajectory, with the grayscale arrows showing the direction and energy of photon emission. (c),(d) Resulting γ-ray beams with $\varepsilon_\gamma > 1$ MeV at incident powers of 1 and 4 PW. The green circles show what we define as lobes.

our setup is the transparency. The transparency condition is defined using a dimensionless parameter that we refer to as the normalized laser amplitude, $a_0 \equiv |e|E_0/(m_e c\omega)$, where m_e and e are the electron mass and charge, ω is the frequency of the laser pulse, and c is the speed of light. In the case of nonrelativistic plasma electrons, the plasma is transparent to the laser pulse if $n_e < n_{cr}$, where $n_{cr} \equiv m_e\omega^2/(4\pi e^2)$ is the classical critical or cutoff density. Plasma electrons become highly relativistic at $a_0 \gg 1$, which is the regime of interest for this paper. In the case of relativistic electrons with a characteristic relativistic factor $\langle\gamma\rangle$, the plasma is transparent to the laser pulse if $n_e < \langle\gamma\rangle n_{cr}$ [39]. The increase in the range of electron density has been termed relativistically induced transparency. Typically, the value of $\langle\gamma\rangle$ resulting from electron heating by a laser pulse with a normalized amplitude a_0 can be estimated as $\langle\gamma\rangle \approx a_0$. Then the condition for relativistic transparency becomes $n_e < a_0 n_{cr}$. Therefore, the plasma produced by the channel material should have $n_e \ll a_0 n_{cr}$ to enable relatively unimpeded propagation of the laser pulse. The plasma produced by the bulk material should have a much higher density to guide the laser beam. The preferred range is $n_e \sim a_0 n_{cr}$ or higher.

As a baseline, we perform a 3D PIC simulation where a 1-PW laser pulse irradiates a structured target whose parameters are chosen based on the criteria discussed above. The parameters of the pulse are shown in Table I. The laser intensity has a Gaussian profile in cross section, and, in the absence of the target, the diameter of the focal spot (FWHM of the intensity) is $w_0 \approx 1.3$ μm. The corresponding laser peak intensity is 5×10^{22} W/cm^2, with $a_0 \approx 190$ for $\lambda = 1$ μm. The structured target consists of a bulk plasma with $n_e = n_{bulk} \equiv 100 n_{cr}$ and a narrow channel with a radius $R_{ch} \approx 0.7 w_0$ and $n_e = n_{ch} \equiv 20 n_{cr}$. The bulk thickness d_{bulk} is fixed at 3.0 μm, but our simulations find that the photon emission is not sensitive to the bulk thickness when $d_{bulk} > 3.0$ μm. The bulk plasma guides the laser beam through the channel because $n_{ch}/n_{cr} \ll a_0$, whereas $n_{bulk}/n_{cr} \sim a_0$. An additional channel-density scan shows that values of n_{ch}/n_{cr} between 10 and 30 provide the best photon yield, so this is why we set $n_{ch} = 20 n_{cr}$. The target material in our simulation is initialized as fully ionized plastic, represented by carbon ions. No ionization takes place during the simulation,

TABLE I. Parameters used in the 3D PIC simulations.

Laser pulse	
Pulse energy	37, 75, 149, 223, and 373 J
Peak intensity	5×10^{22} W/cm^2
a_0	190
Wavelength	$\lambda = 1$ μm
Power	$P = 1, 2, 4, 6,$ and 10 PW
Location of focal plane	$x = 0$ μm
Pulse profile (transverse and longitudinal)	Gaussian
Pulse duration (FWHM of intensity)	35 fs
Focal-spot size (FWHM of intensity)	$w_0 = 1.3, 1.9, 2.7, 3.2$ and 4.2 μm
Plasma	
Composition	Carbon ions and electrons
Bulk density	$n_{bulk} = 100 n_{cr}$
Bulk thickness	$d_{bulk} = 3.0$ μm
Channel density	$n_{ch} = 20 n_{cr}$
Ionization state of carbon	Fully ionized
Channel radius	$R_{ch} = 0.7 w_0$
Channel length	$L_{ch} = 45$ μm
General parameters	
Spatial resolution	30/μm × 30/μm × 30/μm
No. of macroparticles per cell	
Electrons	15
Carbon ions	5

which significantly reduces computational costs during the parameter scans described in later sections of the paper. A simulation with field ionization [40] and initially neutral carbon atoms (instead of ions) reproduces the results reported in this section, which justifies our approach of using fully ionized targets.

In the simulation performed, the laser pulse indeed generates high-energy electrons while propagating through the channel. Figure 6, discussed in later sections, provides a snapshot of the electron spectrum. The maximum electron energy is 450 MeV, which corresponds to $\gamma \approx 900$. This is much higher than the characteristic relativistic factor associated with electron oscillations in the laser pulse, $\langle\gamma\rangle \approx a_0 \approx 190$. The energy increase is aided by the slowly evolving azimuthal magnetic field (approximately 0.2 MT) generated in the channel.

The magnetic field bends the trajectories of the energetic electrons, and the resulting acceleration leads to synchrotron emission [41]. This process is simulated by considering emission of individual photons according to a Monte Carlo algorithm [42–46] that utilizes an appropriate cross section. Our code of choice for these calculations is EPOCH [40]. Note that the photons are emitted along the momentum of the emitting electron.

The emission pattern for photons with $\varepsilon_\gamma > 1$ MeV is shown in Fig. 1(c). In this plot, the photons are projected onto a sphere. The polar angle is measured with respect to the propagation direction of the laser pulse (the dashed circles mark polar angles of 10° and 45°). The horizontal plane is the polarization plane of the laser electric field. The emitted photons are primarily concentrated near this plane, because the polarization plane is also the plane of the electron oscillations driven by the laser electric field. The photon beam has two distinct lobes, offset by similar angles from the direction of propagation of the laser beam. In what follows, we define a lobe more precisely as a cone [green circles in Figs. 1(c) and 1(d)] with an opening angle of 10°. Each lobe is centered at the peak of emission for a given photon energy range, as seen in Figs. 1(c) and 1(d).

In order to quantify the emission process described, we introduce an energy conversion rate for photons with energies above a given threshold emitted into a single lobe. This is defined as the ratio of the energy associated with these photons to the total energy in the incoming laser beam. The conversion rate in Fig. 2(a) is an average of the rates for the right and left lobes for photons with energies above 1, 10, and 100 MeV. On average, a single lobe produced by a 1-PW laser pulse contains 2.3×10^{11} MeV-level photons [shown in Fig. 2(b)], which account for approximately 0.5% of the total laser energy.

III. INCIDENT-POWER SCAN

In this section, we examine how the photon emission changes with the power P of the incident laser pulse. We

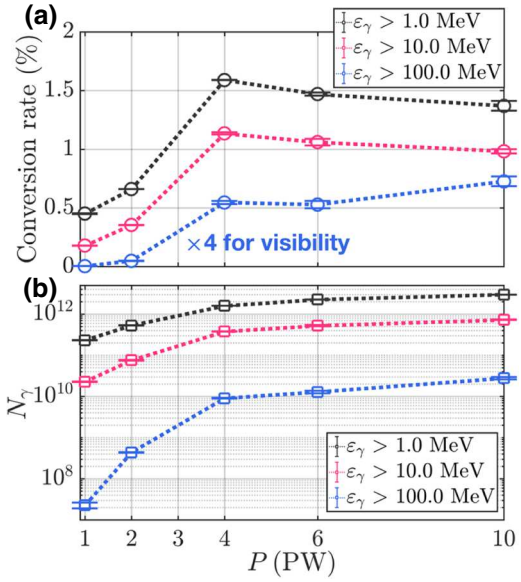

FIG. 2. Efficiency of conversion of laser energy into photons (a) and number of photons emitted into a 10° lobe (b) for different photon energies ($\varepsilon_\gamma > 1, 10$, and 100 MeV) as functions of the incident laser power P at a fixed peak intensity of 5×10^{22} W/cm^2. Both the efficiency and the photon number are averaged over the right and left lobes, with the error bars giving the deviation from the average.

are specifically interested in a regime where the power is increased while the peak intensity remains constant. As pointed out in Refs. [33] and [47], while the peak power of lasers has increased quickly in the past, technical challenges associated with large-aperture laser beams have led to a slower increase in the peak intensity. An intensity of 5×10^{22} W/cm^2 is to be expected as a very realistic value across several of the existing and upcoming multi-PW to 10-PW-class laser facilities [33], such as ELI-NP [35], the Texas PW laser [34], the CoReLS laser [48], and Apollon [49]. In other words, our exploration is a study of laser systems that can reach the same peak intensity but at different levels of incident power.

Figure 2(a) shows the efficiency of conversion of energy into γ rays with energies ε_γ above 1, 10, and 100 MeV as a function of the incident power when it is increased from 1 to 10 PW. As stated in Table I, the incident power is increased by increasing the size of the focal spot and thus the laser energy while keeping the peak intensity and the pulse duration constant. The key result is that the conversion efficiency increases rapidly with P for $P \leq 4$ PW. Broadly speaking, the conversion efficiency saturates above $P \approx 4$ PW. The subtle difference is that the efficiency of conversion into multi-MeV photons decreases slowly, whereas the conversion efficiency for $\varepsilon_\gamma > 100$ MeV continues to increase slowly. The corresponding numbers of photons above the same cutoff energies are given in Fig. 2(b). We find that the number

of multi-MeV photons scales with power roughly as P^2 up to 4 PW and as P beyond 4 PW. Even more dramatically, for photons above 100 MeV, the number is increased by about 400 times with a 4-PW laser and about 1200 times with a 10-PW laser compared with the number for 1 PW, leading to a power scaling of P^4 up to 4 PW. These numbers are critical for explaining the power scaling of pair production in Sec. IV. The variation with power, however, preserves the two-lobe structure of the emitted photon beam, as observed in Figs. 1(c) and 1(d).

In what follows, we examine the key factors contributing to the observed trend in the conversion efficiency. Our core conclusion is that the increase is closely related to improved direct laser acceleration of electrons assisted by the azimuthal magnetic field in the plasma. It is important to point out that, as we increase the incident power, we increase proportionally the number of electrons in the channel. Therefore, the conversion efficiency would remain the same if the emitted power were to increase only due to this increase in the number of electrons. In order to take this aspect into account explicitly, we introduce a renormalized emitted power,

$$\mathcal{P}_\gamma \equiv P_{\text{lobe}} \frac{1\ \text{PW}}{P}, \tag{1}$$

which is the power emitted into a single lobe, P_{lobe}, divided by P, or, equivalently, a factor proportional to w_0^2. An increase in $\mathcal{P}_\gamma$ with power is then a clear indicator of increased efficiency of conversion of energy into photons.

Figure 3 shows the time history of $\mathcal{P}_\gamma$ for photons with $\varepsilon_\gamma > 10$ MeV for $P = 1$–10 PW. We define $t = 0$ fs as the time when the laser pulse reaches its peak amplitude in the focal plane at $x = 0$ μm in the absence of the target. There are two striking features: the peak of the emission $\mathcal{P}_\gamma$ increases significantly as P is increased from 1 to 4 PW, and the emission remains strong over a much longer time period for $P = 4$ and 10 PW. The prolonged emission reflects the fact that the laser depletion is reduced with an increase in laser power. The depletion associated with electron extraction from the channel walls scales as w_0 (surface area per unit length). On the other hand, the energy in the laser pulse scales as w_0^2 (volume per unit length). This is why it takes longer for a laser pulse with higher power to become depleted in our setup, as confirmed by our 3D PIC simulations.

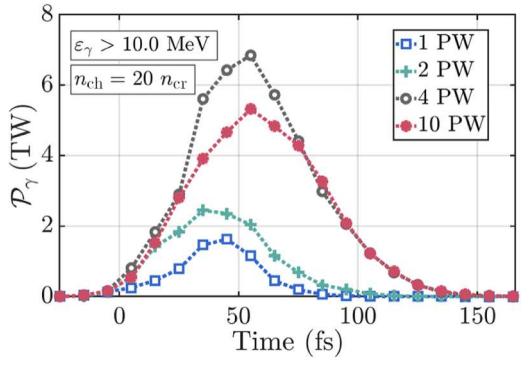

FIG. 3. Normalized emitted power $\mathcal{P}_\gamma$ [see Eq. (1)] as a function of time t at $P = 1$, 2, 4, and 10 PW. $\mathcal{P}_\gamma$ peaks at 45 fs for $P = 1$ PW, at 35 fs for $P = 2$ PW, and at 55 fs for $P = 4$ and 10 PW. The FWHMs of these curves are 33, 50, 55, and 66 fs, respectively.

The prolonged emission definitely increases the conversion efficiency, but the substantial increase in the peak value of $\mathcal{P}_\gamma$ is an equally important contributing factor. There are two aspects that must be considered independently in this context: (1) the power emitted by a single electron, and (2) the number of emitting electrons. In order to be quantitative, we focus on photon emission with $\varepsilon_\gamma >$ 10 MeV into a single lobe as defined in Sec. II.

A. Increased emission by individual electrons

The power P_{synch} of synchrotron emission is determined by the acceleration of an electron in an instantaneous rest frame [41]. This acceleration is proportional to a dimensionless parameter η, defined as

$$\eta \equiv \frac{\gamma_e}{E_S} \sqrt{\left(\mathbf{E} + \frac{1}{c}[\mathbf{v} \times \mathbf{B}]\right)^2 - \frac{1}{c^2}(\mathbf{E} \cdot \mathbf{v})^2}, \tag{2}$$

where $\mathbf{E}$ and $\mathbf{B}$ are the electric and magnetic fields acting on the electron, γ_e and $\mathbf{v}$ are the relativistic factor and the velocity of the electron, and $E_S \approx 1.3 \times 10^{18}$ V/m is the Schwinger field. The power of the synchrotron emission scales as

$$P_{\text{synch}} \propto \eta^2. \tag{3}$$

The spectrum emitted by an electron with a relativistic factor γ_e and a dimensionless parameter η peaks at photon energies roughly given by [50]

$$\varepsilon_\gamma^* \approx 0.44 \eta \gamma_e m_e c^2. \tag{4}$$

An important conclusion that one can draw from this is that the emission of photons with energy ε_γ is strongly suppressed for electrons whose ε_γ^*, calculated according to Eq. (4), is much smaller than ε_γ, i.e., $\varepsilon_\gamma^* \ll \varepsilon_\gamma$.

The two major factors that can increase η are an increase in γ_e and a change in the field configuration. The latter includes not only an increase in the field strength, but also changes in the relative orientation between the electron velocity and the fields. In order to quantify this aspect, we

introduce an effective field strength, defined as

$$\mathcal{F}_{\rm eff} \equiv \frac{1}{E_0}\sqrt{\left(\mathbf{E}+\frac{1}{c}\left[\mathbf{v}\times\mathbf{B}\right]\right)^2-\frac{1}{c^2}\left(\mathbf{E}\cdot\mathbf{v}\right)^2}, \quad (5)$$

so that

$$\eta = \gamma_e \mathcal{F}_{\rm eff} E_0/E_S, \quad (6)$$

where E_0 is the maximum electric field strength of the laser pulse in the absence of the target. We implement detailed tracking of emissions in EPOCH, which allows us to distinguish the changes in η caused by changes in $\mathcal{F}_{\rm eff}$ and γ_e of the emitting electrons. Specifically, we record the position and momentum of each photon at the moment of emission together with the corresponding η and γ_e of the emitting electron.

Figure 4 details how the emitted power $\mathcal{P}_\gamma$ depends on $\mathcal{F}_{\rm eff}$ and γ_e at the peak of the emission for photons with $\varepsilon_\gamma > 10$ MeV. Even though the typical $\mathcal{F}_{\rm eff}$ changes very little with the incident power P, the energies of the emitting electrons increase substantially. For $P = 4$ and 10 PW, most of the emissions are performed by electrons with $\varepsilon_\gamma^* > 10$ MeV, corresponding to the data points to the right of the curve, where ε_γ^* is the characteristic photon energy

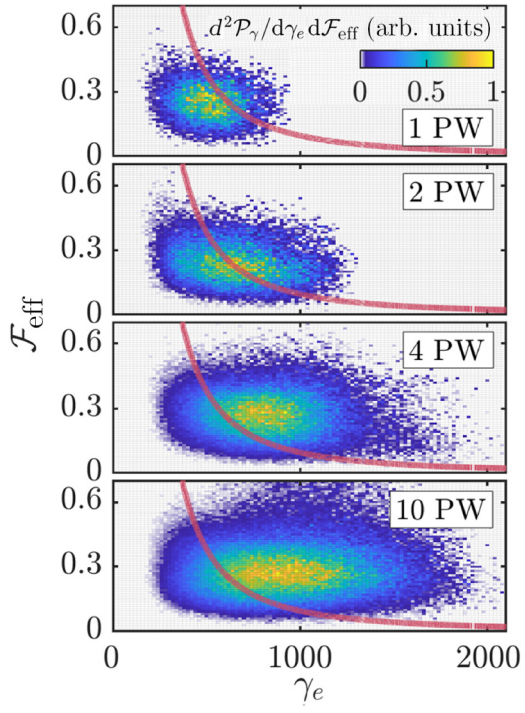

FIG. 4. Emitted power $\mathcal{P}_\gamma$ as a function of $\mathcal{F}_{\rm eff}$ and γ_e at the time of peak emission (see Fig. 3) for $P = 1$–10 PW. $\mathcal{P}_\gamma$ is for photons with $\varepsilon_\gamma > 10$ MeV emitted into a single lobe. The curve corresponds to $\varepsilon_\gamma^* = 10$ MeV [see Eq. (4)].

of the synchrotron spectrum defined by Eq. (4). This qualitative change is the reason for the visible increase in $\mathcal{P}_\gamma$ at $P \geq 4$ PW as compared with $P = 1$ PW.

Our observation regarding the importance of the increase in electron energy is further substantiated by Fig. 5. To aid comparison, all curves here are normalized such that the area under each curve is equal to unity. Figure 5(a) shows that the effective field strength $\mathcal{F}_{\rm eff}$ at the time of maximum emission increases from 0.24 at 1 PW to only 0.29 at 10 PW. This means that the field configuration sampled by the electrons remains relatively unchanged with this increase in power. In contrast, the typical γ_e of the emitting electrons almost doubles at 10 PW compared with that at 1 PW, as shown in Fig. 5(b).

The fact that $\mathcal{F}_{\rm eff}$ remains primarily unaffected is consistent with the current understanding of direct laser acceleration in a quasistatic magnetic field. The field limits the amplitude of transverse electron displacement across the channel even when the electron energy increases [14]. The maximum displacement is often referred to as the magnetic boundary. The maximum magnetic field sampled by the electron, i.e., the field at the magnetic boundary, scales

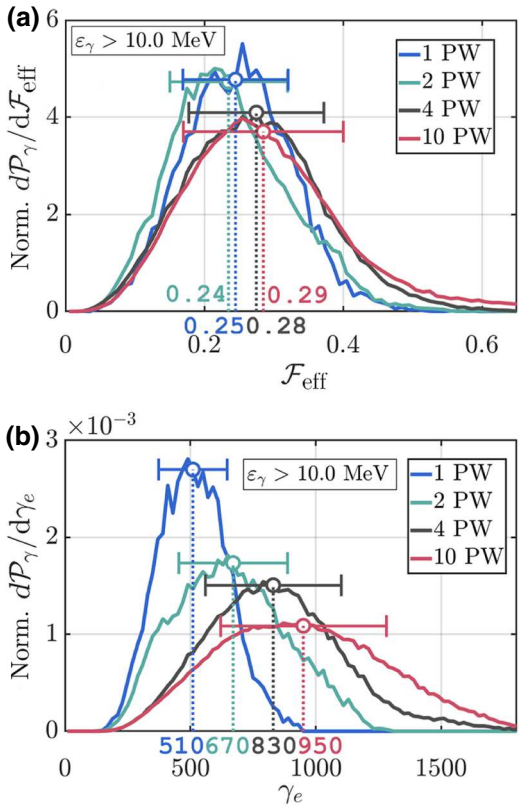

FIG. 5. Emitted power $\mathcal{P}_\gamma$ for photons with $\varepsilon_\gamma > 10$ MeV emitted into a single lobe as a function of (a) $\mathcal{F}_{\rm eff}$ and (b) γ_e at the time of peak emission (see Fig. 3) for $P = 1$–10 PW. The dashed lines show the average $\mathcal{F}_{\rm eff}$ and γ_e. The horizontal bars show the standard deviation. The area under each curve is normalized to be equal to unity.

as $j^{1/2}$, where j is the characteristic current density. We observe no increase in j with an increase in P, which explains the trend shown in Fig. 5(a). The momentum acquired during electron injection from the channel walls into the laser beam also impacts on the size of the magnetic boundary and it likely contributes to the variations observed in Fig. 5(a).

Rather than directly influencing $\mathcal{F}_{\text{eff}}$, the role of the magnetic field is more subtle. The magnetic field facilitates energy exchange of the electrons with the laser pulse. Even though the electrons experience similar values of $\mathcal{F}_{\text{eff}}$ during acceleration, the duration of this interaction increases with the laser power. As already stated, it takes longer for the laser beam to become depleted at higher power, which prolongs the time the electrons spend being accelerated by the laser pulse. However, the depletion time competes with the dephasing time, which also limits the energy gain [14]. Therefore, the depletion eventually loses its importance with increasing power, once the corresponding time becomes relatively long. Note that an increase in γ_e causes an increase in η even though $\mathcal{F}_{\text{eff}}$ remains relatively unaffected. For example, the average η for the emissions shown in Fig. 4 almost doubles as the power is increased from 1 to 10 PW, reaching $\eta \approx 0.12$.

B. Increased number of emitting electrons

The increase in the energy conversion efficiency results not only from increased emission by individual electrons, but also from an increase in the number of emitting electrons beyond just the geometric factor. This increase is in part related to radial electron confinement. The transverse displacement of the electrons has to be less than the channel radius in order for the electrons not to become lost while being accelerated. As we increase the channel radius in our power scan, we improve the electron confinement, as confirmed by particle tracking, which then allows significantly more electrons to reach higher energies at 4 PW than at 1 PW.

Figure 6(a) shows the electron spectra at the time of maximum emission for $P = 1$–10 PW. We count only the electrons whose momentum $\mathbf{p}_e$ is directed into the emission cone, because the photons are emitted collinearly with $\mathbf{p}_e$. The number of electrons N_e is normalized to account for the increase in the channel radius, with the normalized number defined as

$$\tilde{N}_e \equiv N_e \frac{1\ \text{PW}}{P}. \tag{7}$$

The number of energetic electrons increases strongly as the incident power rises from 1 to 2 PW and from 2 to 4 PW. There is also a clear saturation at $P \geq 4$ PW, with the 4- and 10-PW spectra being very similar.

It is also instructive to evaluate the electrons according to ε_γ^*, defined by Eq. (4), where ε_γ^* is the characteristic photon energy of the synchrotron spectrum for given values of γ_e and η. Figure 6(b) shows the total number of electrons with $\varepsilon_\gamma^* > \varepsilon_\gamma$ as a function of ε_γ, where

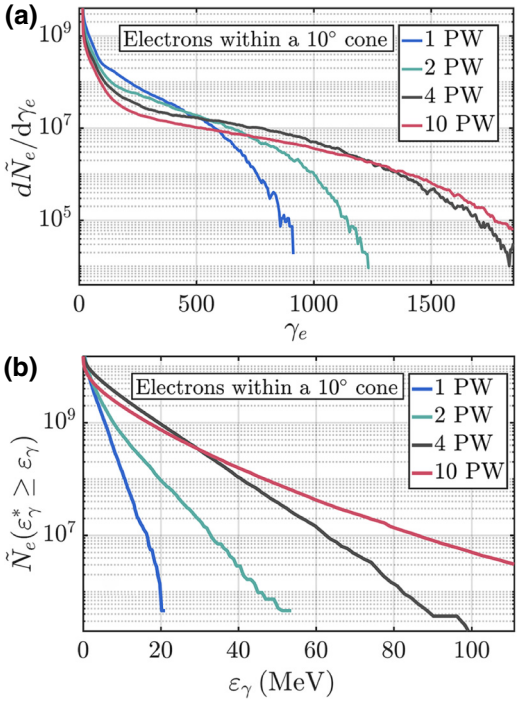

FIG. 6. (a) Normalized electron spectra at the moment of peak emission for $P = 1$–10 PW. (b) Accumulated number of electrons with $\varepsilon_\gamma^* > \varepsilon_\gamma$, defined by Eq. (8), as a function of ε_γ. Here $\varepsilon_\gamma^* \approx 0.44\eta\gamma_e m_e c^2$ is the characteristic photon energy of a synchrotron spectrum. We count only the electrons whose momentum is directed within a single emission lobe.

$$\tilde{N}_e(\varepsilon_\gamma^* \geq \varepsilon_\gamma) \equiv \int_{\varepsilon_\gamma}^{\infty} \frac{d\tilde{N}_e}{d\varepsilon_\gamma^*} d\varepsilon_\gamma^*. \tag{8}$$

We find that $\tilde{N}_e(\varepsilon_\gamma^* \geq 1\ \text{MeV})$ for $P = 4$ PW significantly exceeds $\tilde{N}_e(\varepsilon_\gamma^* \geq 1\ \text{MeV})$ for $P = 1$ PW, which contributes to the increase in the conversion efficiency shown in Fig. 2(a). Figure 6(b) also shows that there are slightly more electrons with $\varepsilon_\gamma^* > 1$ MeV and $\varepsilon_\gamma^* > 10$ MeV at $P = 4$ PW than at $P = 10$ PW. This is why the conversion efficiency for $\varepsilon_\gamma > 1$ MeV and $\varepsilon_\gamma > 10$ MeV decreases above $P = 4$ PW. This trend changes for $\varepsilon_\gamma > 100$ MeV because the 10-PW beam is able to generate more electrons with ε_γ^* above 30 MeV.

IV. CREATION OF ELECTRON-POSITRON PAIRS VIA TWO-PHOTON COLLISIONS

In the previous section, we show that the number of MeV-level photons ($\varepsilon_\gamma > 1$ MeV) emitted into a narrow cone with an opening angle of 10° grows rapidly with the incident laser power until it reaches saturation at around

4 PW. Multiple applications can potentially benefit from such a strong scaling with power, e.g., two-photon pair production, radiography of ultrahigh-density matter, and photonuclear reactions [51]. In this section, we examine in detail one of these—photon-photon pair production or, equivalently, the generation of matter and antimatter directly from light. Here we investigate two different approaches to achieving two-photon pair production: one is to collide two γ-ray beams, and the other is to collide one γ-ray beam with a high-temperature black-body radiation field [38].

First, we consider the setup schematically shown in Fig. 7(a), which was discussed in Ref. [32] and detailed in Refs. [52] and [53]. The two colliding γ-ray beams are collimated beams emitted into single 10° lobes. The collision occurs in vacuum at a distance d that greatly exceeds the spatial scales associated with photon emission within a single structured target. MeV-level photons are absolutely necessary for pair production via collisions of two photons (the linear Breit-Wheeler process [54]) because, in order to successfully generate pairs, the photon energies must satisfy the requirement $\varepsilon_{\gamma 1}\varepsilon_{\gamma 2} > 2m_e^2c^4$, where $\varepsilon_{\gamma 1}$ and $\varepsilon_{\gamma 2}$ are the energies of the colliding photons. Because of this requirement and the existence of highly energetic photons ($\varepsilon_\gamma > 100$ MeV), the energy threshold for dumping photons is lowered in our simulations to 10 keV.

To calculate the production of pairs via the linear Breit-Wheeler (BW) process [54], we discretize the photons in each beam into energy bins and collide the photon bins in one beam with those in the other. For two colliding bins with energies $\varepsilon_{\gamma_{1,2}}$ and photon numbers $N_{\gamma_{1,2}}$, the number of pairs generated can be estimated as

$$N_{\text{pairs}} \approx \sigma_{\gamma_1\gamma_2} N_{\gamma_1} N_{\gamma_2}/\pi\theta^2 d^2, \tag{9}$$

where $\sigma_{\gamma_1\gamma_2}$ is the cross section for the BW process [54], and $\theta = 10^\circ$ is the divergence angle of the photon beam. We collect the pairs generated in all possible binary collisions to get the total number of pairs.

As an example, we calculate the number of pairs obtained by colliding two γ-ray beams produced by two 4-PW lasers. In our calculation, the collision distance is $d = 250$ μm and the collision angle is $\Phi = 90^\circ$. The total number of pairs generated is 12 620. Figure 7(b) shows the distribution of BW pairs over the energy bins of the two γ-ray beams. The axes are defined as $s_\gamma \equiv \log_{10}(\varepsilon_\gamma/\text{MeV})$ to make the low-energy photons' contribution visible. As claimed earlier, the MeV-level photons are indeed necessary, because pair production involving MeV-level photons accounts for more than 98% of the total yield (these are reactions where at least one photon has $\varepsilon_\gamma > 1$ MeV). However, an unexpected result is that pair production involving photons with $\varepsilon_\gamma < 1$ MeV also accounts for a significant fraction—nearly 85% (these are reactions where one of the photons has $\varepsilon_\gamma < 1$ MeV). So, in our setup, photons with both $\varepsilon_\gamma < 1$ MeV and $\varepsilon_\gamma > 1$ MeV are indispensable for pair production. Since most of the pairs are produced in collisions where $\varepsilon_{\gamma_1} \gg \varepsilon_{\gamma_2}$ or $\varepsilon_{\gamma_2} \gg \varepsilon_{\gamma_1}$, the positrons are emitted as two highly collimated beams that are collinear with the original photon beams, as shown in Fig. 7(a).

Because of the reliance on both low- and high-energy photons, the increase in the number of pairs with the laser power [the red curve in Fig. 7(c)] depends not only on the power scaling of the number of high-energy photons [see Fig. 2(b)], but also on that of the low-energy photons. As shown in Fig. 7(c) and detailed in its caption, the number of pairs grows rapidly up to 4 PW, with an average scaling of $P^{2.4}$, whereas the growth rate drops quickly beyond 4 PW, reaching a scaling of $P^{1.1}$ at 10 PW. According to the trend observed in Fig. 2(b), the number of MeV-level

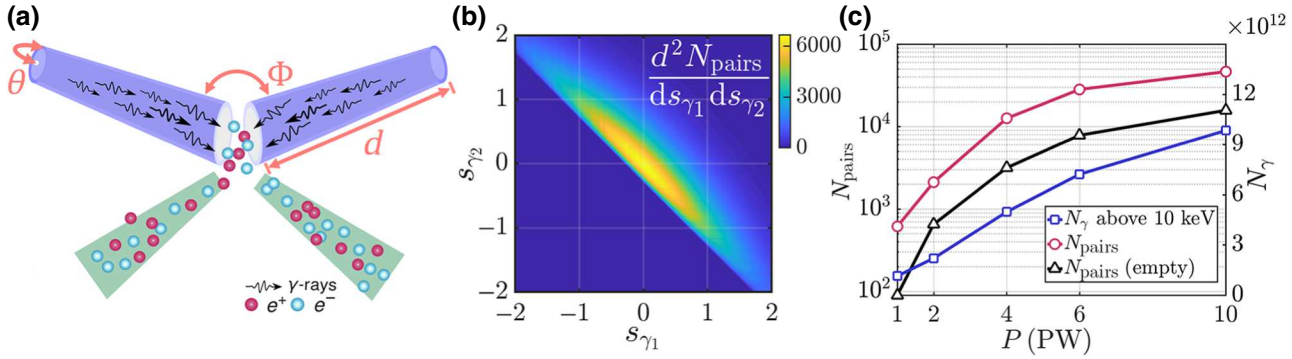

FIG. 7. (a) Setup for pair production via two-photon collisions in two intersecting γ-ray beams, where θ is the beam divergence angle, Φ is the collision angle, and d is the collision distance. (b) Distribution of BW pairs with respect to the energies of the two colliding photon beams, with $s_\gamma \equiv \log_{10}(\varepsilon_\gamma/\text{MeV})$. The laser power producing each of the photon beams is 4 PW, and the collision distance is 250 μm. (c) Pair production versus the laser power used to generate each of the photon beams. The blue curve shows the number of colliding photons (in each beam) with energies above 10 keV. The number of pairs scales with power as $P^{2.3}$, $P^{2.6}$, $P^{1.9}$, and $P^{1.1}$ as we increase P from 1 to 2 PW, 2 to 4 PW, 4 to 6 PW, and 6 to 10 PW. The black curve shows the pair yield for empty channels.

photons increases roughly as P^2 for laser powers up to 4 PW, and so the scaling for pairs would be P^4 if pair production involved only MeV-level photons. This discrepancy means that the number of low-energy photons increases with P at a slower rate, which is exactly what the blue curve of Fig. 7(c) manifests.

Next, we investigate the approach of colliding one γ-ray beam with high-temperature black-body radiation. Figure 8(a) depicts the proposed setup, where the black-body radiator (e.g., a laser-heated *hohlraum*) is hundreds of eV in temperature and 1 cm in thickness. As detailed in Ref. [38], the number of pairs generated is the product of the absorption probability per unit length τ and the thickness of the black body, where τ depends strongly on the temperature of the black-body radiation. Here we initialize the black-body radiation with three distinct temperatures, $T = 100$, 200, and 400 eV. When colliding a γ-ray beam generated by a 4-PW laser pulse with this black-body radiation, we obtain 1.2×10^5 pairs for $T = 400$ eV, 800 pairs for $T = 200$ eV, and just 2 pairs for $T = 100$ eV. It has to be pointed out that these numbers are upper limits on the possible numbers of pairs because the angular spread of the γ-ray beam is not included in the calculation.

By binning the generated pairs according to the energies of the γ-ray photons, it is easy to see which part of the photon spectrum contributes most to pair production. For example, Fig. 8(b) demonstrates that the energies between 50 and 500 MeV dominate the production when the γ-ray beam collides with 400-eV black-body radiation. Similar effects are also observed when $T = 100$ and 200 eV, except that the center of the energy range shifts further up with a decrease in temperature. The sole reliance on the highly energetic γ-ray photons is an important feature that distinguishes the setup considered here from the one considered earlier in this section. This aspect changes the scaling of the number of pairs with the incident laser power. As illustrated in Fig. 8(c) and explained in its caption, for $T = 400$ eV the number of pairs increases with power as $P^{4.5}$ for P up to 4 PW. The scaling matches the trend in the number of photons with energies above 100 MeV, shown in Fig. 2(b). This is a much stronger scaling than the scaling obtained for the collision of two γ-ray beams, and can benefit the detection of two-photon pair production by significantly increasing the signal-to-noise ratio. The power scaling at $T = 100$ and 200 eV [see Fig. 8(c)] is cut off at lower powers due to negligible pair production, whereas the remaining part resembles the power scaling at 400 eV. Finally, it must be stressed that the number of generated pairs depends sensitively on the black-body temperature. As shown in Fig. 8(c), decreasing the temperature by a factor of 2 can result in a reduction in the number of pairs by more than 2 orders of magnitude. Such a temperature sensitivity poses potential challenges for experimental implementations of this approach.

We conclude this section by pointing out that the targets with prefilled channels considered above yield appreciably more electron-positron pairs than do structured targets with empty channels. The use of empty channels has generated significant interest [55–57], so, in order to make a meaningful comparison, we repeat the power scan using an empty channel. In our PIC simulations, we set $n_{\rm ch} = 0$ and lengthen the channel to accommodate the prolonged laser propagation in empty channels. Specifically, we set $L_{\rm ch} = 120$ μm for 1, 2, and 4 PW and $L_{\rm ch} = 200$ μm for 6 and 10 PW. At 1–6 PW, the laser pulse contains less than 10% of its initial energy when it approaches the end of the extended tube. At 10 PW, this number is 30%. All other simulation parameters are the same as in Table I. Figure 9 shows the number of γ-ray photons emitted into a 10° lobe and the corresponding conversion efficiency. Note that for an empty channel the 10° cone surrounds the emission peak, whereas the emission pattern does not always have a two-lobe structure. We use the emitted photons to calculate the pair yield obtained via the two approaches discussed

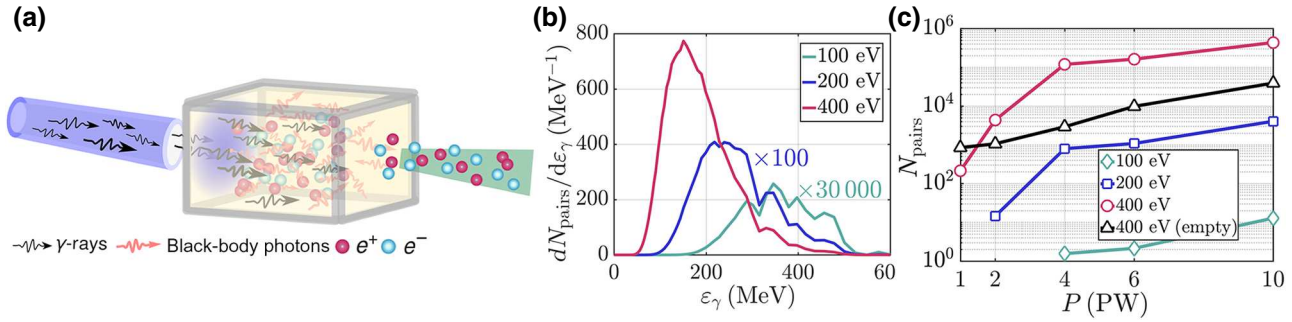

FIG. 8. (a) Setup for two-photon pair production via collision of an intense γ-ray beam with high-temperature radiation from a laser-heated *hohlraum*. (b) Pair production as a function of γ-ray energy. A γ-ray beam (enclosed within a 10° lobe) generated by a 4-PW laser collides with 100-, 200-, and 400-eV black-body radiators. To make the curves for 100 and 200 eV visible, the y axes are multiplied by 3×10^4 and 100, respectively. (c) Pair production versus the laser power used to generate the γ-ray beam. At 400 eV, the number of pairs scales with power as $P^{4.3}$, $P^{4.8}$, $P^{0.8}$, and $P^{2.0}$ as we increase P from 1 to 2 PW, 2 to 4 PW, 4 to 6 PW, and 6 to 10 PW, respectively. The black curve shows the pair yield for an empty channel.

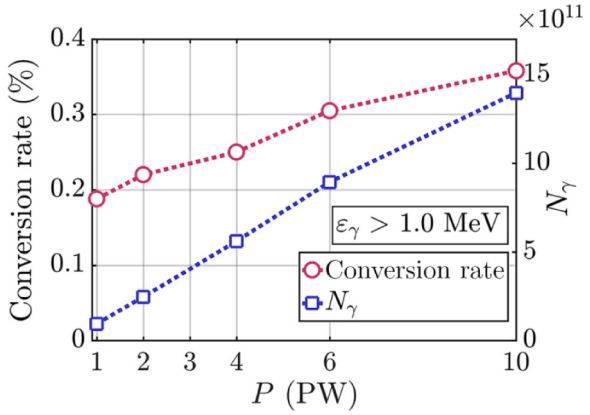

FIG. 9. Number of γ-ray photons ($\varepsilon_\gamma > 1.0$ MeV) emitted into a 10° lobe and the corresponding conversion efficiency in a power scan for an empty channel.

above. The results are shown in Figs. 7(c) and 8(c). It is evident that the prefilled channel outperforms the empty channel in both photon production and pair yield. Taking $P = 4$ PW as an example, we find that only 0.25% of the laser energy is converted into MeV-level photons (and 0.3% into photons above 10 keV) within a 10° lobe. When two such γ-ray beams collide, they produce 3150 BW pairs, which is four times lower than the yield for prefilled channels. When one such γ-ray beam collides with 400-eV black-body radiation, it produces 2920 BW pairs, which is 41 times smaller than the yield for the prefilled-channel target.

In this section, we compare two approaches (i.e., colliding two γ-ray beams and colliding one γ-ray beam with black-body radiation) to generating BW pairs, utilizing γ-ray sources driven by multi-PW lasers. We find that the two approaches are somewhat comparable in terms of the pairs produced, but the process involves different parts of the energy spectrum of the γ-ray beam and depends sensitively on the parameters assumed. As a result, the approach of colliding a γ-ray beam with black-body radiation has a stronger scaling with the incident laser power, but the number of generated pairs can drop exponentially with a decrease in the black-body temperature.

V. SUMMARY AND DISCUSSION

We examine the emission of collimated γ-ray beams from structured laser-irradiated targets with prefilled cylindrical channels. Our goal is to determine how the efficiency of conversion of the laser energy into γ rays scales with the incident laser power or incident laser energy (since the duration of the laser pulse is fixed) when the peak intensity is held constant. We find that the efficiency of conversion into MeV-level ($\varepsilon_\gamma > 1$ MeV) photons increases rapidly with the incident laser power in the range between 1 and 4 PW before it roughly saturates above $P \approx 4$ PW. The setup considered, involving a structured target, becomes an efficient and powerful γ-ray source when irradiated by a 4-PW laser pulse at 5×10^{22} W/cm^2, with 1.6% of the laser energy converted into 1.6×10^{12} MeV-level photons within a 10° lobe.

Our detailed particle tracking reveals that the underlying cause of the improved conversion efficiency is enhanced electron acceleration by the laser pulse, assisted by the quasistatic magnetic field generated in the channel. This is a nontrivial result, because the laser intensity and thus a_0 in the incoming laser pulse remain unchanged. Another peculiar aspect revealed by our analysis is that the characteristic effective field $\mathcal{F}_{\text{eff}}$ experienced by the emitting electrons in the channel undergoes only minor changes as the channel widens. The delayed laser depletion and the improved transverse electron confinement by the magnetic field are believed to play a significant role in improving electron acceleration at higher power P.

Applying the γ-ray beams generated in our 3D simulations, we carry out a numerical study of electron-positron pair creation via two-photon collisions. Up to 1.2×10^5 pairs are created when one γ-ray beam generated at $P =$ 4 PW is shot into black-body radiation at 400 eV. The number of pairs scales strongly with laser power, namely, $N_{\text{pairs}} \propto P^{4.5}$ for $P \leq 4$ PW, because the most energetic γ-ray photons ($\varepsilon_\gamma > 50$ MeV) control the yield. However, the pair production depends greatly on the black-body temperature; e.g., if the temperature is reduced by a factor of 2, the number of pairs drops by a factor of 100. Another approach is to collide two identical γ-ray beams, which leads to an average scaling of $P^{2.4}$ at $P \leq 4$ PW. The yield is 12 620 pairs at 4 PW with a collision distance of 250 μm. The weaker scaling is due to the coupling of low-energy ($\varepsilon_\gamma < 1$ MeV) and high-energy ($\varepsilon_\gamma > 1$ MeV) photons during the pair creation process. The power scaling discovered above is nontrivial and can provide useful guidelines for designing future two-photon experiments using state-of-the-art laser facilities.

In addition, we examine the pair yield generated by γ rays in empty channels. It has been reported that empty channels produce highly collimated γ-ray beams with just a single lobe aligned with the direction of laser propagation [56]. However, this emission pattern is achieved by artificially treating the ions as immobile [58], so that energetic electrons surf longitudinally along the channel without transverse oscillations [59]. In simulations using the correct charge-to-mass ratio of the ions, the motion of the ions disrupts electron acceleration and degrades the collimation of the emission pattern [60]. In contrast, prefilled structured targets offer a robust setup for efficient generation of γ-ray beams. The resulting beams produce significantly more pairs, which indicates that targets with prefilled channels are superior candidates for experiments aimed at two-photon pair production with the laser parameters considered, i.e., a multi-PW laser with an intensity of

around 5×10^{22} W/cm^2 and a pulse duration of more than 30 fs.

Photon sources are often characterized using their brilliance, so, in order to provide a point of reference, we evaluate this parameter for the γ-ray beam generated at $P = 4$ PW. In our calculation, the central photon energy is $\varepsilon_\gamma = 1$ MeV, and we consider only the photons emitted into a single 10° lobe. The source size given by the spatial standard deviation is approximately 2×1 μm^2, and the divergence angle characterizing the source is approximately 0.7 rad. Using these values, we obtain a peak brilliance of 3×10^{23} photons/s mm^2 mrad^2 0.1% BW (at 1.0 MeV). However, it is important to point out that the merits of brilliance should be viewed in connection with a specific application. In the case of pair production, the spectral brightness characterized by the brilliance is less important than the total number of high-energy photons. As already shown, our beams, which have a broad spectrum ranging from tens of keV to hundreds of MeV, are capable of producing a significant number of pairs that is impossible to achieve using conventional γ-ray sources.

ACKNOWLEDGMENTS

This research was supported by the NSF (Grants No. 1632777 and No. 1821944) and AFOSR (Grant No. FA9550-17-1-0382). We acknowledge financial support from the French National Research Agency (Grant No. ANR-17-CE30-0033-01) TULIMA Project. Simulations were performed with EPOCH (developed under UK EPSRC Grants EP/G054950/1, EP/G056803/1, EP/G055165/1 and EP/ M022463/1) using high performance computing resources provided by TACC at the University of Texas. This work used XSEDE, supported by NSF Grant No. ACI-1548562. Data collaboration was supported by the SeedMe2 project.

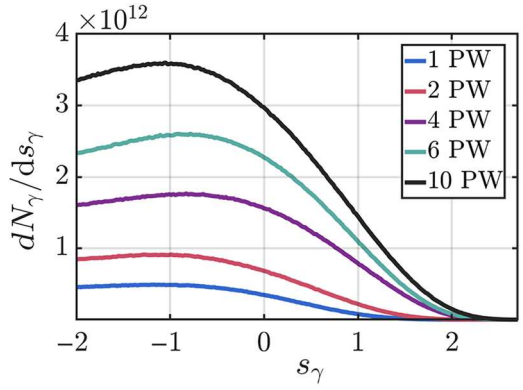

FIG. 10. Energy spectra of γ-ray beams generated with different laser powers. Here, "γ-ray beam" still refers to the photons emitted into a narrow cone with an opening angle of 10°. We use $s_\gamma \equiv \log_{10}(\varepsilon_\gamma/\text{MeV})$ to cover a wide range of energies ε_γ.

APPENDIX: PHOTON ENERGY SPECTRUM FOR γ-RAY BEAMS

In Fig. 2(b), we report the number of photons in the γ-ray beams investigated above three distinct energy thresholds, i.e., 1, 10, and 100 MeV. However, it is still necessary to present continuous photon energy spectra for these γ-ray beams, since the pair yield depends on the spectral shape. Figure 10 illustrates the photon spectral distribution from 10 keV to 500 MeV for all of the laser powers explored. To make the low-energy part of the spectrum visible, the variable ε_γ is replaced by $s_\gamma \equiv \log_{10}(\varepsilon_\gamma/\text{MeV})$.

[1] C. Pellegrini, A. Marinelli, and S. Reiche, The physics of x-ray free-electron lasers, Rev. Mod. Phys. **88**, 015006 (2016).

[2] C. Pellegrini, X-ray free-electron lasers: From dreams to reality, Phys. Scr. **T169**, 014004 (2016).

[3] E. Schneidmiller and M. Yurkov, in *Proc. of International Free Electron Laser Conference (FEL'17), Santa Fe, NM, USA, August 20–25, 2017*, 38 (JACoW, Santa Fe, 2018), p. 109.

[4] J. Bahrdt and E. Gluskin, Cryogenic permanent magnet and superconducting undulators, Nucl. Instrum. Methods Phys. Res. Sect. A **907**, 149 (2018).

[5] B. F. Lasinski, A. B. Langdon, S. P. Hatchett, M. H. Key, and M. Tabak, Particle-in-cell simulations of ultra intense laser pulses propagating through overdense plasma for fast-ignitor and radiography applications, Phys. Plasmas **6**, 2041 (1999).

[6] S. Bulanov, V. Bychenkov, V. Chvykov, G. Kalinchenko, D. Litzenberg, T. Matsuoka, A. Thomas, L. Willingale, V. Yanovsky, K. Krushelnick, *et al.*, Generation of GeV protons from 1 PW laser interaction with near critical density targets, Phys. Plasmas **17**, 043105 (2010).

[7] S. Palaniyappan, B. Hegelich, H. Wu, D. Jung, D. Gautier, L. Yin, B. Albright, R. Johnson, T. Shimada, S. Letzring, *et al.*, Dynamics of relativistic transparency and optical shuttering in expanding overdense plasmas, Nat. Phys. **8**, 763 (2012).

[8] D. Stark, C. Bhattacharjee, A. Arefiev, T. Toncian, R. D. Hazeltine, and S. Mahajan, Relativistic Plasma Polarizer: Impact of Temperature Anisotropy on Relativistic Transparency, Phys. Rev. Lett. **115**, 025002 (2015).

[9] J. Fernández, C. Gautier, C. Huang, S. Palaniyappan, B. Albright, W. Bang, G. Dyer, A. Favalli, J. Hunter, J. Mendez, *et al.*, Laser-plasmas in the relativistic-transparency regime: Science and applications, Phys. Plasmas **24**, 056702 (2017).

[10] T. Nakamura, S. Bulanov, T. Esirkepov, and M. Kando, High-Energy Ions from Near-Critical Density Plasmas via Magnetic Vortex Acceleration, Phys. Rev. Lett. **105**, 135002 (2010).

[11] D. Stark, T. Toncian, and A. Arefiev, Enhanced multi-MeV Photon Emission by a Laser-Driven Electron Beam in a Self-Generated Magnetic Field, Phys. Rev. Lett. **116**, 185003 (2016).

[12] O. Jansen, T. Wang, D. Stark, E. d'Humières, T. Toncian, and A. Arefiev, Leveraging extreme laser-driven magnetic fields for gamma-ray generation and pair production, Plasma Phys. Control. Fusion **60**, 054006 (2018).

[13] T. Wang, T. Toncian, M. S. Wei, and A. V. Arefiev, Structured targets for detection of Megatesla-level magnetic fields through Faraday rotation of XFEL beams, Phys. Plasmas **26**, 013105 (2019).

[14] Z. Gong, F. Mackenroth, T. Wang, X. Yan, T. Toncian, and A. Arefiev, Forward sliding-swing acceleration: electron acceleration by high-intensity lasers in strong plasma magnetic fields, arXiv:1811.00425 (2018).

[15] Z. Gong, F. Mackenroth, X. Yan, and A. Arefiev, Strong energy enhancement in a laser-driven plasma-based accelerator through stochastic friction, arXiv:1905.02152 (2019).

[16] B. Liu, H. Wang, J. Liu, L. Fu, Y. Xu, X. Yan, and X. He, Generating Overcritical Dense Relativistic Electron Beams via Self-Matching Resonance Acceleration, Phys. Rev. Lett. **110**, 045002 (2013).

[17] M. Vranic, R. Fonseca, and L. Silva, Extremely intense laser-based electron acceleration in a plasma channel, Plasma Phys. Control. Fusion **60**, 034002 (2018).

[18] T. Nakamura, J. Koga, T. Esirkepov, M. Kando, G. Korn, and S. Bulanov, High-Power γ-Ray Flash Generation in Ultraintense Laser-Plasma Interactions, Phys. Rev. Lett. **108**, 195001 (2012).

[19] C. Ridgers, C. Brady, R. Duclous, J. Kirk, K. Bennett, T. Arber, A. Robinson, and A. Bell, Dense Electron-Positron Plasmas and Ultraintense γ Rays from Laser-Irradiated Solids, Phys. Rev. Lett. **108**, 165006 (2012).

[20] L. Ji, A. Pukhov, E. Nerush, I. Y. Kostyukov, B. Shen, and K. Akli, Energy partition, γ-ray emission, and radiation reaction in the near-quantum electrodynamical regime of laser-plasma interaction, Phys. Plasmas **21**, 023109 (2014).

[21] T. Blackburn, C. P. Ridgers, J. G. Kirk, and A. Bell, Quantum Radiation Reaction in Laser–Electron-Beam Collisions, Phys. Rev. Lett. **112**, 015001 (2014).

[22] J. Li, K. Hatsagortsyan, B. Galow, and C. Keitel, Attosecond Gamma-Ray Pulses via Nonlinear Compton Scattering in the Radiation-Dominated Regime, Phys. Rev. Lett. **115**, 204801 (2015).

[23] H. Chang, B. Qiao, T. Huang, Z. Xu, C. Zhou, Y. Gu, X. Yan, M. Zepf, and X. He, Brilliant petawatt gamma-ray pulse generation in quantum electrodynamic laser-plasma interaction, Sci. Rep. **7**, 45031 (2017).

[24] X. Zhu, M. Chen, T. Yu, S. Weng, L. Hu, P. McKenna, and Z. Sheng, Bright attosecond γ-ray pulses from nonlinear Compton scattering with laser-illuminated compound targets, Appl. Phys. Lett. **112**, 174102 (2018).

[25] T. Huang, C. Kim, C. Zhou, M. Cho, K. Nakajima, C. Ryu, S. Ruan, and C. Nam, Highly efficient laser-driven Compton gamma-ray source, New J. Phys. **21**, 013008 (2019).

[26] F. Mackenroth and A. Di Piazza, Nonlinear Compton scattering in ultrashort laser pulses, Phys. Rev. A **83**, 032106 (2011).

[27] A. Gonoskov, A. Bashinov, S. Bastrakov, E. Efimenko, A. Ilderton, A. Kim, M. Marklund, I. Meyerov, A. Muraviev, and A. Sergeev, Ultrabright GeV Photon Source via Controlled Electromagnetic Cascades in Laser-Dipole Waves, Phys. Rev. X **7**, 041003 (2017).

[28] J. Snyder, L. Ji, K. George, C. Willis, G. Cochran, R. Daskalova, A. Handler, T. Rubin, P. Poole, D. Nasir, *et al.*, Relativistic laser driven electron accelerator using micro-channel plasma targets, Phys. Plasmas **26**, 033110 (2019).

[29] A. Haid, L. Carlson, N. Alexander, B. Russ, A. Forsman, J. Oakdale, and S. Chenen, Millimeter-scale seamless 2-photon polymerization additive manufacturing, Poster presentation in the 2019 Target Fabrication Conference: https://tfab19.lle.rochester.edu/ (2019).

[30] J. Williams, Private communications at General Atomics, 2019.

[31] E. Gaul, T. Toncian, M. Martinez, J. Gordon, M. Spinks, G. Dyer, N. Truong, C. Wagner, G. Tiwari, M. Donovan, T. Ditmire, and B. Hegelich, Improved pulse contrast on the Texas Petawatt Laser, J. Phys.: Conf. Ser. **717**, 012092 (2016).

[32] X. Ribeyre, E. d'Humières, O. Jansen, S. Jequier, V. Tikhonchuk, and M. Lobet, Pair creation in collision of γ-ray beams produced with high-intensity lasers, Phys. Rev. E **93**, 013201 (2016).

[33] C. N. Danson, C. Haefner, J. Bromage, T. Butcher, J.-C. F. Chanteloup, E. A. Chowdhury, A. Galvanauskas, L. A. Gizzi, J. Hein, D. I. Hillier, *et al.*, Petawatt and exawatt class lasers worldwide, High Power Laser Sci. Eng. **7**, e54 (2019).

[34] G. Tiwari, E. Gaul, M. Martinez, G. Dyer, J. Gordon, M. Spinks, T. Toncian, B. Bowers, X. Jiao, R. Kupfer, L. Lisi, E. McCary, R. Roycroft, A. Yandow, G. Glenn, M. Donovan, T. Ditmire, and B. Hegelich, Beam distortion effects upon focusing an ultrashort petawatt laser pulse to greater than 10^22 W/cm^2, Opt. Lett. **44**, 2764 (2019).

[35] D. Ursescu, G. Chériaux, P. Audebert, M. Kalashnikov, T. Toncian, M. Cerchez, M. Kaluza, G. Paulus, G. Priebe, R. Dabu, M. Cernaianu, M. Dinescu, T. Asavei, I. Dancus, L. Neagu, A. Boianu, C. Hooker, C. Barty, and C. Haefner, Laser beam delivery at ELI-NP, Rom. Rep. Phys. **68**, 11 (2016).

[36] A. Pukhov, Z. Sheng, and J. Meyer-ter Vehn, Particle acceleration in relativistic laser channels, Phys. Plasmas **6**, 2847 (1999).

[37] A. Arefiev, V. Khudik, A. Robinson, G. Shvets, L. Willingale, and M. Schollmeier, Beyond the ponderomotive limit: Direct laser acceleration of relativistic electrons in sub-critical plasmas, Phys. Plasmas **23**, 056704 (2016).

[38] O. Pike, F. Mackenroth, E. Hill, and S. Rose, A photon–photon collider in a vacuum hohlraum, Nat. Photonics **8**, 434 (2014).

[39] P. Gibbon, *Short Pulse Laser Interactions with Matter* (World Scientific Publishing Company, Singapore, 2004). Chap. 5.

[40] T. Arber, K. Bennett, C. Brady, A. Lawrence-Douglas, M. Ramsay, N. Sircombe, P. Gillies, R. Evans, H. Schmitz, A. Bell, *et al.*, Contemporary particle-in-cell approach to laser-plasma modelling, Plasma Phys. Control. Fusion **57**, 113001 (2015).

[41] L. Landau and E. Lifshitz, *The Classical Theory of Fields* (Butterworth-Heinemann, Oxford, 1987). Chap. *9*.

[42] R. Duclous, J. Kirk, and A. Bell, Monte Carlo calculations of pair production in high-intensity laser-plasma interactions, Plasma Phys. Control. Fusion **53**, 015009 (2010).

[43] I. Sokolov, J. Nees, V. Yanovsky, N. Naumova, and G. Mourou, Emission and its back-reaction accompanying electron motion in relativistically strong and QED-strong pulsed laser fields, Phys. Rev. E **81**, 036412 (2010).

[44] N. Elkina, A. Fedotov, I. Kostyukov, M. Legkov, N. Narozhny, E. Nerush, and H. Ruhl, QED cascades induced by circularly polarized laser fields, Phys. Rev. ST Accel. Beams **14**, 054401 (2011).

[45] C. Ridgers, J. Kirk, R. Duclous, T. Blackburn, C. Brady, K. Bennett, T. Arber, and A. Bell, Modelling gamma-ray photon emission and pair production in high-intensity laser–matter interactions, J. Comput. Phys. **260**, 273 (2014).

[46] A. Gonoskov, S. Bastrakov, E. Efimenko, A. Ilderton, M. Marklund, I. Meyerov, A. Muraviev, A. Sergeev, I. Surmin, and E. Wallin, Extended particle-in-cell schemes for physics in ultrastrong laser fields: Review and developments, Phys. Rev. E **92**, 023305 (2015).

[47] T. Ditmire, High-power Lasers: The invention of the laser 50 years ago has led to the latest generation of devices, with power bursts thousands of times that of the nation's entire electrical grid, Am. Sci. **98**, 394 (2010).

[48] J. W. Yoon, C. Jeon, J. Shin, S. K. Lee, H. W. Lee, I. W. Choi, H. T. Kim, J. H. Sung, and C. H. Nam, Achieving the laser intensity of $5.5 \times 10^2 2\mathrm{W/cm}^2$ with a wavefront-corrected multi-PW laser, Opt. Express **27**, 20412 (2019).

[49] D. Papadopoulos, J. Zou, C. Le Blanc, G. Chériaux, P. Georges, F. Druon, G. Mennerat, P. Ramirez, L. Martin, A. Fréneaux, *et al.*, The Apollon 10 PW laser: Experimental and theoretical investigation of the temporal characteristics, High Power Laser Sci. Eng. **4**, e34 (2016).

[50] A. R. Bell and J. G. Kirk, Possibility of Prolific Pair Production with High-Power Lasers, Phys. Rev. Lett. **101**, 200403 (2008).

[51] W. Bertozzi, J. A. Caggiano, W. K. Hensley, M. S. Johnson, S. E. Korbly, R. J. Ledoux, D. P. McNabb, E. B. Norman, W. H. Park, and G. A. Warren, Nuclear resonance fluorescence excitations near 2 MeV in ^{235}U and ^{239}Pu, Phys. Rev. C **78**, 041601 (2008).

[52] X. Ribeyre, E. d'Humières, O. Jansen, S. Jequier, and V. T. Tikhonchuk, Electron–positron pairs beaming in the Breit–Wheeler process, Plasma Phys. Control. Fusion **59**, 014024 (2016).

[53] X. Ribeyre, E. d'Humières, S. Jequier, and V. T. Tikhonchuk, Effect of differential cross section in Breit–Wheeler pair production, Plasma Phys. Control. Fusion **60**, 104001 (2018).

[54] G. Breit and J. Wheeler, Collision of two light quanta, Phys. Rev. J. **46**, 1087 (1934).

[55] L. Yi, A. Pukhov, P. Luu-Thanh, and B. Shen, Bright X-Ray Source from a Laser-Driven Microplasma Waveguide, Phys. Rev. Lett. **116**, 115001 (2016).

[56] J. Yu, R. Hu, Z. Gong, A. Ting, Z. Najmudin, D. Wu, H. Lu, W. Ma, and X. Yan, The generation of collimated γ-ray pulse from the interaction between 10 PW laser and a narrow tube target, Appl. Phys. Lett. **112**, 204103 (2018).

[57] J. Yu, H. Lu, T. Takahashi, R. Hu, Z. Gong, W. Ma, Y. Huang, C. Chen, and X. Yan, Creation of Electron-Positron Pairs in Photon-Photon Collisions Driven by 10-PW Laser Pulses, Phys. Rev. Lett. **122**, 014802 (2019).

[58] J. Yu, Ion charge to mass ratio, Private Communications (2019).

[59] Z. Gong, A. Robinson, X. Yan, and A. Arefiev, Highly collimated electron acceleration by longitudinal laser fields in a hollow-core target, Plasma Phys. Control. Fusion **61**, 035012 (2019).

[60] T. Wang, Z. Gong, K. Chin, and A. Arefiev, Impact of ion dynamics on laser-driven electron acceleration and gamma-ray emission in structured targets at ultra-high laser intensities, Plasma Phys. Control. Fusion **61**, 084004 (2019).